Water Research 253 (2024) 121290

Contents lists available at ScienceDirect

Water Research

journal homepage: www.elsevier.com/locate/watres

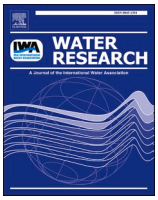

Superhydrophobic sand evaporator with core-shell structure for long-term salt-resistant solar desalination

Qingyang Xue [a,b], Peng Xiao [b], Jincui Gu [b,*], Wenqin Wang, Characterization [a,*], Luke Yan [c], Tao Chen [b,*]

[a] School of Materials Science and Chemical Engineering, Ningbo University, Ningbo 315211, China
[b] Key Laboratory of Marine Materials and Related Technologies, Zhejiang Key Laboratory of Marine Materials and Protective Technologies, Ningbo Institute of Material Technology and Engineering, Chinese Academy of Science, Ningbo 315201, China
[c] Polymer Materials & Engineering Department, School of Materials Science & Engineering, Chang' an University, Xi'an 710064, China

ARTICLE INFO

Keywords:
Solar evaporator
Superhydrophobicity
Core-shell structure
Salt-resistant
Environmental stability

ABSTRACT

Solar-driven water evaporation, as an environmentally benign pathway, provides an opportunity for alleviating global clean water scarcity. However, the rapidly generated interfacial steam and localized heating could cause increased salt concentration and accumulation, deteriorating the evaporation performance and long-term stability. Herein, a novel superhydrophobic sand solar (FPPSD) evaporator with a core-shell structure was proposed through interface functionalization for continuous photothermal desalination. The collective behavior essence of the sand aggregate gave itself micron-scale self-organized pores and configurable shapes, generating desirable capillary force and supplying effective water-pumping channels. More importantly, combining the dopamine, polypyrrole (PPy), and 1H,1H,2H,2H-perfluorodecyltriethoxysilane (PFDTS) through π-π conjugation and multiple hydrogen bonding effects gave the FPPSD evaporator with stable superhydrophobic property and highly efficient photothermal conversion capability. Therefore, the FPPSD evaporator showed a continuous and stable photothermal performance even after 96 h continuous evaporation under 3-sun irradiation for 10 wt% saline solution, among the best values in the reported works of literature, demonstrating its excellent salt-resistance stability. Furthermore, this novel FPPSD evaporator displayed outstanding environmental stability that kept its initial water transport capacity even after being treated under harsh conditions for 30 days. With excellent salt-resistance ability and stable environmental stability, the FPPSD evaporator will provide an attractive platform for sustainable solar-driven water management.

1. Introduction

The freshwater crisis became a severe global concern during modern society's development. To alleviate clean water scarcity, solar vapor generations (SVGs) have demonstrated exciting opportunities for developing eco-friendly freshwater harvesting (Li et al., 2021a; Tao et al., 2018; Zhao et al., 2020). The photothermal material is a crucial member to determine light-to-heat conversion ability during the evaporation process (Cheng et al., 2022; Ding et al., 2021; Huang et al., 2022; Li et al., 2023a; Yu et al., 2023; Yang et al., 2023a). Nowadays, tremendous efforts have been devoted to developing photothermal materials, such as membranes, aerogels, hydrogels, biomass materials, carbon-based foams, and plasmonic nanoparticles (Cao et al., 2023; Fan et al., 2020; Jia et al., 2019; Lu et al., 2020; Mu et al., 2019a, 2019b; Shi et al., 2021; Wang et al., 2020; Wang et al., 2021a; Xie et al., 2023; Xing et al., 2023; Yang et al., 2023b; Zhang et al., 2019; Zhao et al., 2022; Zou et al., 2023). Meanwhile, highly localized photothermal heating at the evaporation surface can be realized through interfacial evaporator design to maximize solar utilization and suppress heat loss to the bulk water (Li et al., 2021b; Xu et al., 2020). Nevertheless, due to the increased salt accumulation, most existing photothermal materials suffer from restricted solar desalination performance (Chen et al., 2023a; Zhang et al., 2023a). The crystallized salt was inherently prone to the salt clogging the microchannels of SVGs during the evaporation process, which may compromise the sunlight absorption and undermine the water transport and result in the dramatical deterioration of evaporation performance, and ultimately stopping the SVGs system (Xu et al., 2023a; Liu et al., 2023).

* Corresponding authors.
E-mail addresses: gujincui@nimte.ac.cn (J. Gu), wangwenqin@nbu.edu.cn (W. Wang), tao.chen@nimte.ac.cn (T. Chen).

https://doi.org/10.1016/j.watres.2024.121290
Received 21 November 2023; Received in revised form 11 January 2024; Accepted 7 February 2024
Available online 8 February 2024

Various attempts have been proposed to achieve steady evaporation, such as mechanical moving and force-driven fluid flow to enhance ion migration (Dong et al., 2022; Razaqpur et al., 2021; Zhang et al., 2021a). Additionally, various superhydrophobic evaporators have been recently designed to meet this challenge by tuning water transport in the photothermal layer (Hu et al., 2020; Lai et al., 2023; Li et al., 2021c; Wu et al., 2020; Xu et al., 2021; Xie et al., 2022; Shen et al., 2020; Wang et al., 2023a). Xu et al. fabricated a superhydrophobic carbon nanotubes-based membrane for solar desalination. Under one sun, this device displayed an evaporation rate of ~1.41 kg m^{-2} h^{-1} after 40 h (Shen et al., 2020). Wu et al. demonstrated a polyethylene/graphene nanosheet foam with interconnected channels and surface micro-nanostructures. It exhibited an evaporation rate of ~1.83 kg m^{-2} h^{-1} and can keep its property under high temperatures and acid-/alkali solutions (Xie et al., 2022). Also, Janus evaporators were constructed to improve the salt-resistance ability of solar desalination (Chen et al., 2020a; Li et al., 2022; Paternò et al., 2022; Zhang et al., 2022a). Xu et al. developed a Janus evaporator for durable desalination of hypersaline water. It displayed good durability for the 20 wt% NaCl with no salt accumulation after continuous evaporation for 5 days (9 h one day in the simulated daytime) (Li et al., 2022). Tang et al. fabricated a Janus solar interfacial evaporator with 3D biomimetic architecture for stable solar energy evaporation. It can achieve rapid and steady long-term evaporation abilities without any salt accumulation (Paternò et al., 2022). Li et al. demonstrated a solar evaporator with a vast water supply pathway and a trapezoidal evaporation surface, and it can keep consecutive evaporation for 14 days (Pan et al., 2023). Although many strategies have been suggested to improve salt-resistance ability, they are usually only used availably under low salinity conditions and low or natural light intensity (Li et al., 2023b; Mo et al., 2022;Wang et al., 2021b; Zang et al., 2021; Zhang et al., 2023b; Zou et al., 2021). Rare studies reported a stable evaporator utilized to resist salt accumulation with high salinity under higher sun illumination. Furthermore, constructing photothermal SVGs systems with high resistance to environmental corrosion is still a critical concern for long-term cyclic evaporation (Wang et al., 2023b; Ni et al., 2020).

Herein, a superhydrophobic sand solar (FPPSD) evaporator was proposed by designing and optimizing the core-shell structure (Scheme 1). The rough surface of the etched sand (SD) particles provided sufficient active sites for subsequent functionalization. Moreover, the abundant hydrophilic functional groups endowed the SD with water-attraction ability. Furthermore, the SD can spontaneously form micrometer-scale pores with configurable shapes and generate ideal capillary interaction, which can serve as an efficient pumping channel for SVGs (Ni et al., 2020). In addition, experimental and theoretical simulation revealed that the polydopamine (PDA) can firmly anchor on the sand surface and serve as an effective binder between the polypyrrole (PPy), and 1H,1H,2H,2H-perfluorodecyltriethoxysilane (PFDTS) through π-π conjugation and multiple hydrogen bonding effects (Scheme 1**a** and **b**) (Yang et al., 2021; Zhang et al., 2021b). Besides, the raw sand has the advantages of wide source and low price, which will be very beneficial for practical application. Therefore, the obtained FPPSD evaporator demonstrated excellent photothermal evaporation performance and salt-resistance ability even after a 96-hour continuous evaporation under 3-sun irradiation for 10 wt% saline solution without any salt crystallization (Scheme 1**c**). In addition, such a novel FPPSD evaporator showed outstanding environmental stability, maintaining its water transport capacity even after being operated under harsh conditions for 30 days, such as strong acid and base, humid acid, glucose, and bull serum albumin system. We hope this work can provide an innovative evaporator design with excellent salt-resistance ability and stable environmental stability for sustainable solar-driven desalination.

2. Material and methods

2.1. Materials

The sand particles (SD) were provided from Ningbo Longfa Fire Engineering Co. LTD. Dopamine hydrochloride, ferric chloride ($FeCl_3{\cdot}6H_2O$), tris-(hydroxymethyl) aminomethane (Tris), pyrrole monomer, hydrochloric acid (HCl), Sodium hydroxide (NaOH) and 1H,1H,2H,2H-perfluorodecyltriethoxysilane (PFDTS, $C_{16}H_{19}F_{17}O_3Si$) were purchased from Aladdin (Shanghai) Co. Ltd. Others were bought from Sigma-Aldrich Co. Ltd.

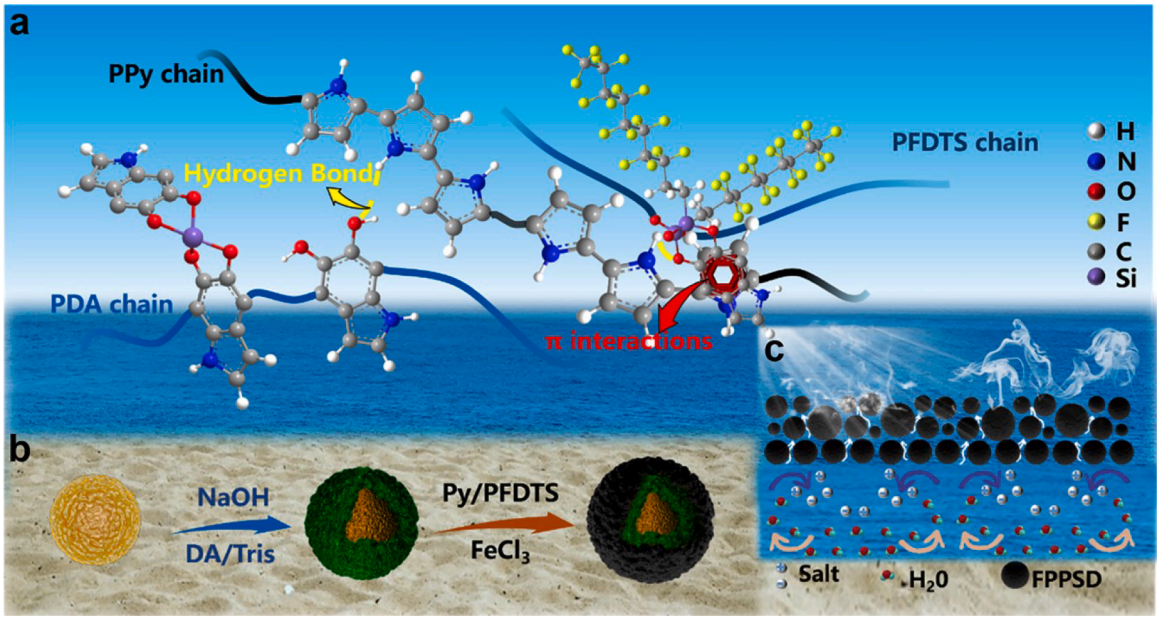

Scheme 1. Schematic illustration of the superhydrophobic sand evaporator with core-shell structure for enhanced solar interface photothermal evaporation. (a) The functionalization of dopamine, PPy, and PFDTS through π-π conjugation and multiple hydrogen bonding effects. (b) The interface modification of the sand particles through the pretreatment with sodium hydroxide and dopamine, and the functionalization of PPy and PFDTS. (c) The salt resistance mechanism of the superhydrophobic FPPSD evaporator for continuous photothermal evaporation.

2.2. Preparation of dopamine/tris mixture solution

2.43 g of Tris was added to deionized water (200 mL) by magnetic stirring. 14.85 mL of 0.1 M HCl was used to adjust the pH was 8.5. Then, the above solution was fixed to 400 mL with deionized water to obtain the Tris buffer solution. Finally, 0.8 g of dopamine hydrochloride was evenly dispersed in the Tris buffer solution under the dark condition to form the dopamine/tris (DA/Tris) solution.

2.3. Preparation of the superhydrophobic FPPSD with a core-shell structure

The superhydrophobic FPPSD was prepared through the *in-situ* oxygen polymerization method. Firstly, the sands were cleaned with deionized water and anhydrous ethanol under ultrasonic conditions for 1 h, respectively and dried. Secondly, the sands were ultrasonicated in NaOH solution (0.5 M) for 2 h, and cleaned with deionized water. Thirdly, the NaOH-treated sand was added into the DA/Tris mixture and continuously stirred at 40 ℃ for 14 h to allow DA/Tris to polymerize *in situ* on the sand surface to obtain the PDA functionalized sand (PDSD). The PDSD was repeatedly washed with deionized water and annealed under 90 ℃. Lastly, the PDSD was stirred in the PFDTS/pyrrole (4 wt%) mixture for 1 h, and then reacted with $FeCl_3$ aqueous solution (0.5 M) for 8 h to obtain the PFDTS/PPy/PDA@sand (FPPSD). For comparison, PFDTS/PPy/sand (FPYSD) was obtained by *in-situ* polymerization of PFDTS and PPy directly on the NaOH-treated sand surface under the abovementioned conditions.

2.4. Preparation of the solar-driven FPPSD evaporator device

Petri dish ($d = 35$ mm, $h = 12$ mm) was selected as the container for solar-driven evaporation. The FPPSD was added inside the container and can float on water surface due to the superhydrophobic property. To explore the effect of FPPSD loading on the evaporation effect, different loading amounts (0.75 g, 1.00 g, 1.25 g, 1.50 g, 2.00 g) of FPPSD were used as the photothermal layer.

3. Result and discussion

3.1. Microstructure and chemical structure of FPPSD

The superhydrophobic FPPSD evaporator was fabricated through progressive functionalization. Firstly, the raw SD with average size of ~140 μm was pre-treated with NaOH solution to get a relatively rough surface, guaranteeing steady polymers anchor onto the surface of SD (**Fig. S1**) (Ni et al., 2020). Subsequently, PDA was used to modify the sand surface to get the PDSD via multiple hydrogen bonds, endowing the SD with enhanced light absorption capacity. Finally, the PDSD was modified with PPy and PFDTS through van der Waals interactions and hydrogen bonds to achieve the desirable superhydrophobic FPPSD evaporator with a core-shell structure (**Fig. S2**). As illustrated in Fig. 1**a**, the raw SD was yellow with a particular cluster. However, after the functionalization of SD with PDA, the PDSD became dark green macroscopically. Lastly, the FPPSD turned black when PPy and PFDTS were decorated onto the PDSD. Moreover, the scanning electron microscop (SEM) image of the SD surface dramatically changed at a microscopic scale (Fig. 1**b**). In addition, numerous self-organized pores with a diameter of ~45 μm appeared on the SD aggregate, enabling it to have remarkable water-wicking ability through the capillary effect (Fig. 1**c**) (Ni et al., 2020). Furthermore, the water contact angle (WCA) measurement was explored to explore the wetting behavior. As displayed in Fig. 1**b,** it took <0.01 s for water to penetrate the internal network of the SD aggregate due to its capillary force and superhydrophilicity (**Movie S1**). After PDA modification, the PDSD became

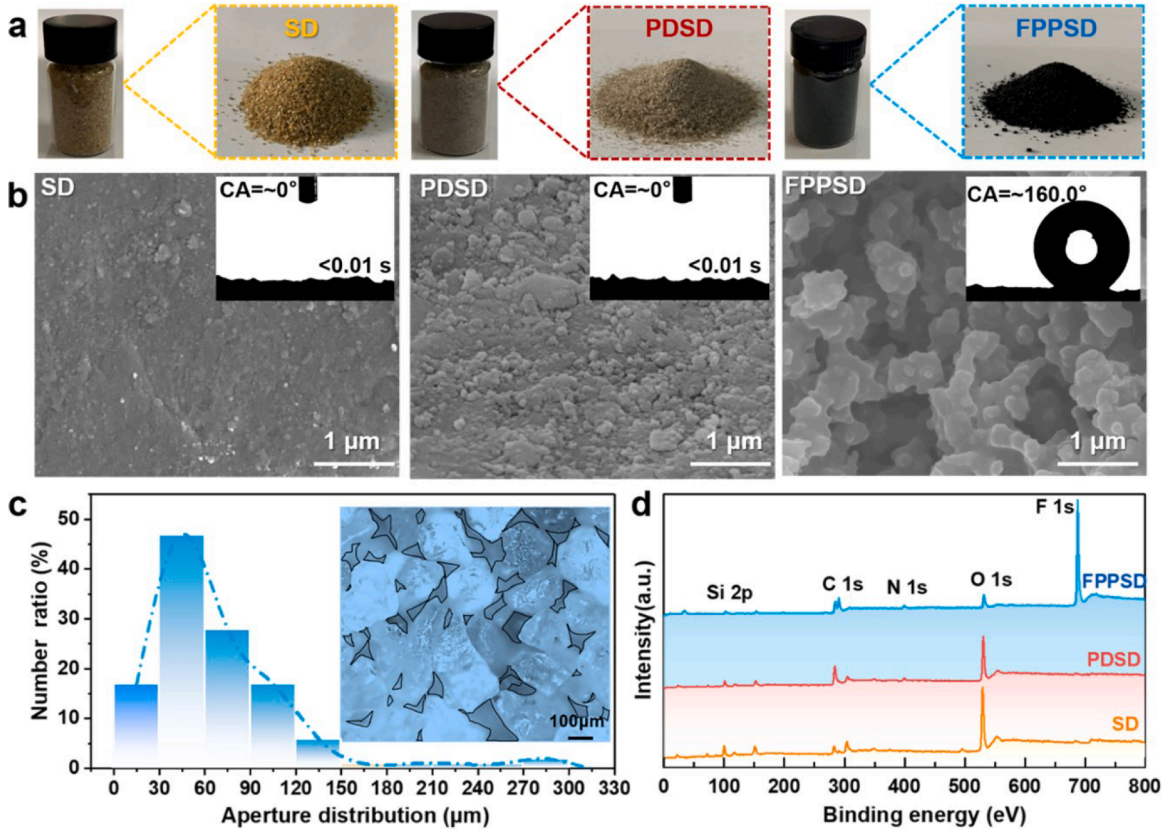

Fig. 1. (a) The photographs of the SD, PDSD and FPPSD (from left to right). (b) The SEM images of the SD, PDSD and FPPSD (Inserting: the WCA of the SD, PDSD and FPPSD, respectively). (c) The diameters distribution of the SD aggregates with self-organized pores. (d) XPS results of the SD, PDSD and FPPSD, respectively.

more hydrophilic because of the abundant hydroxyl functional groups of the PDA (**Movie S2**). In comparison, the FPPSD became superhydrophobic with a WCA of ~160 °C after the functionalization of PFDTS. It wasn't easy to adhere the water molecule to the FPPSD surface (**Fig. S3, Movie S3**), demonstrating its superhydrophobic property and the core-shell structure.

X-ray photoelectron spectroscopy (XPS) characterization was further implemented to clarify the element changes. As shown in Fig. 1**d**, among these three samples, the SD has a high Si peak and a litter N signal was observed. However, a remarkable N peak occurred in the PDSD and FPPSD, and the intensity of the N peak assumed an increasing trend (Wang et al., 2023d). Moreover, the O peak intensity decreased after the decoration of PDA and PPy (Ni et al., 2020). Furthermore, it was noted that the F element appeared at the peak of ~689 eV, indicating the functionalization of the PFDTS (Fig. 2**a, Table S1**) (Park et al., 2003). Meanwhile, the energy dispersive X-ray spectroscopy (EDS) further proved the modification of PDA and PFDTS (**Fig. S4** and **S5)**. The low surface energy and core-shell structure of the FPPSD will provide robust conditions for continuous and stable photothermal evaporation. Moreover, the SD modified with PPy and PFDTS (FPYSD) was also constructed to prove the bridging effect of PDA between the SD, PPy, and PFDTS. XPS was also used to explore the FPPSD and FPYSD chemical information. Fig. 2**b** showed that the C 1 s signal peaks of FPPSD can be divided into four peaks at ~285.0 eV, ~287.6 eV, ~291.5 eV, and ~293.6 eV, standing for C-C, C-N, C-O, and C-F, respectively (Greczynski and Hultman 2020). In comparison, the C-C peak of the FPYSD moved towards the lower binding energy (**Fig. S6**).

Similarly, the N 1 s peaks of FPYSD can be divided into two peaks at ~399.8 eV and ~401.6 eV, corresponding to C-N-C and N-H, respectively (Lazar et al., 2019). After modifying the PDA molecules, the N 1 s peaks shifted into the higher binding energy (Fig. 2**c, S6**). These results indicated that introducing the PDA molecules can improve the binding force of the FPPSD (Lin et al., 2018; Thakur et al., 2014; Wang et al., 2017). Furthermore, Gromacs molecular dynamics simulation (MD) was carried out to verify the interaction between PDA and PPy (**Section S1**). It was found that these two polymer chains were not connected straight as usual but formed a core-shell coating structure (Fig. 2**d**). At the same time, the negative energy between the PDA and PPy molecules indicated that they were attracted to each other, which was also consistent with our hypothesis (Fig. 2**e** and **f**). Besides, with the process of modification of PDA and PPy, the vibration peaks of Si and O disappeared gradually in the Raman spectrum, which better verified the core-shell structure mentioned above (the functional group covered the sand to form a "shell" that was impenetrable by laser). Moreover, compared with the FPYSD, the vibration frequency of the C=C bond was reduced in the Raman spectra of the FPPSD, indicating the introduction of PDA gave more significant structural and chemical stability, which benefited from the electron effect of π-π conjugated interaction between PDA and PPy (Fig. 2**g** and **h**).

3.2. Solar vapor generation

The capacity to absorb light is of the utmost importance for determining the solar-to-thermal conversion performance. As reflected in Fig. 3**a**, the SD has ~60.45 % absorption of total solar energy (wavelength of 400~2500 nm). It can be observed that the modification of PDA and PPy can significantly enhance the light absorption capacity of the FPPSD (~94.63 %) due to the enhancement of the light scattering of the FPPSD aggregate. Furthermore, the solar-to-thermal conversion ability of the FPPSD with different mass loading was studied. As shown in **Fig. S7**, With the increasing mass of the FPPSD, the thickness of the photothermal layer gradually became larger (FPPSD-0.75 g~0.80 mm,

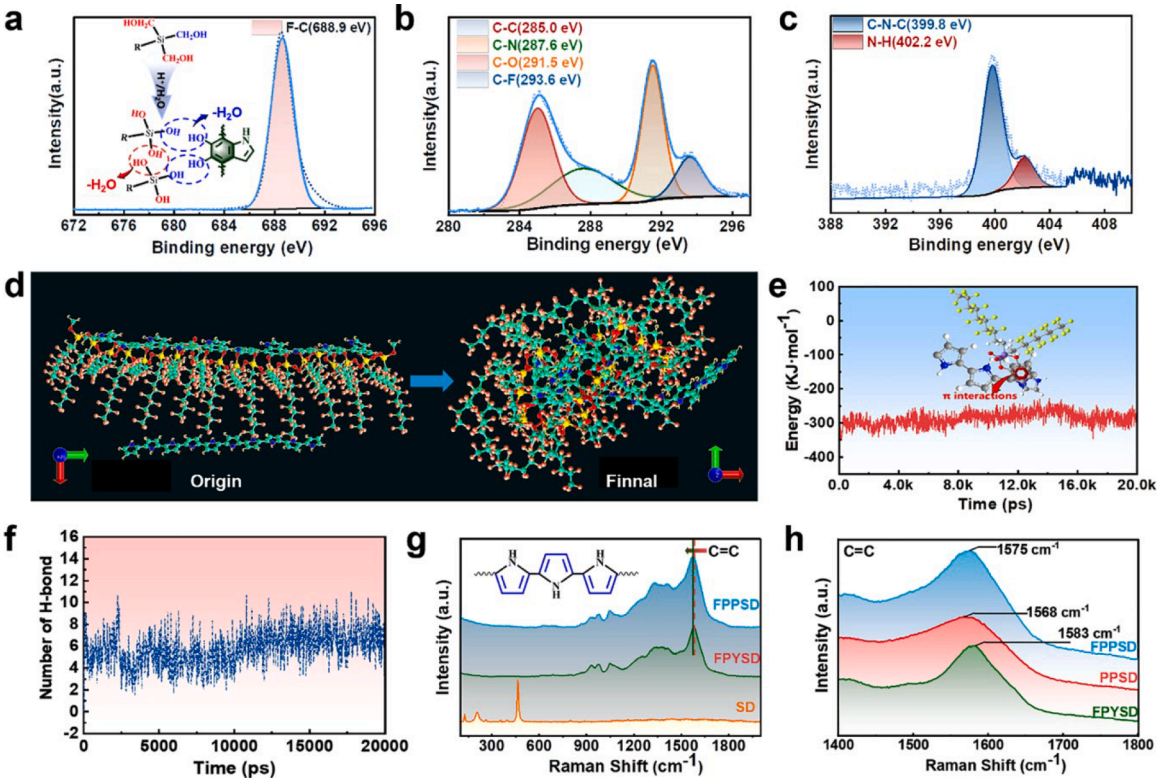

Fig. 2. (a) F1s spectrogram of the FPPSD particles. (b) C1s spectrogram of the FPPSD. (c) N1s spectrogram of the FPPSD. (d) MD simulation process of the intermolecular force between PPy and PDA chain in the FPPSD, the green, red, blue, pink, and white atoms represented C, O, N, F, and H elements, respectively. (e) MD simulation result of the intermolecular force between PPy and PDA chain in the FPPSD. The white, blue, red, yellow, gray, and purple atoms represented H, N, O, F, C, and Si elements, respectively. (f) MD simulation of the H-bond number of the PPy and PDA chain in the FPPSD. (g) Raman spectra of the SD, FPPSD, and FPYSD, respectively. (g) Raman spectra of the PPSD, FPPSD, and FPYSD, respectively.

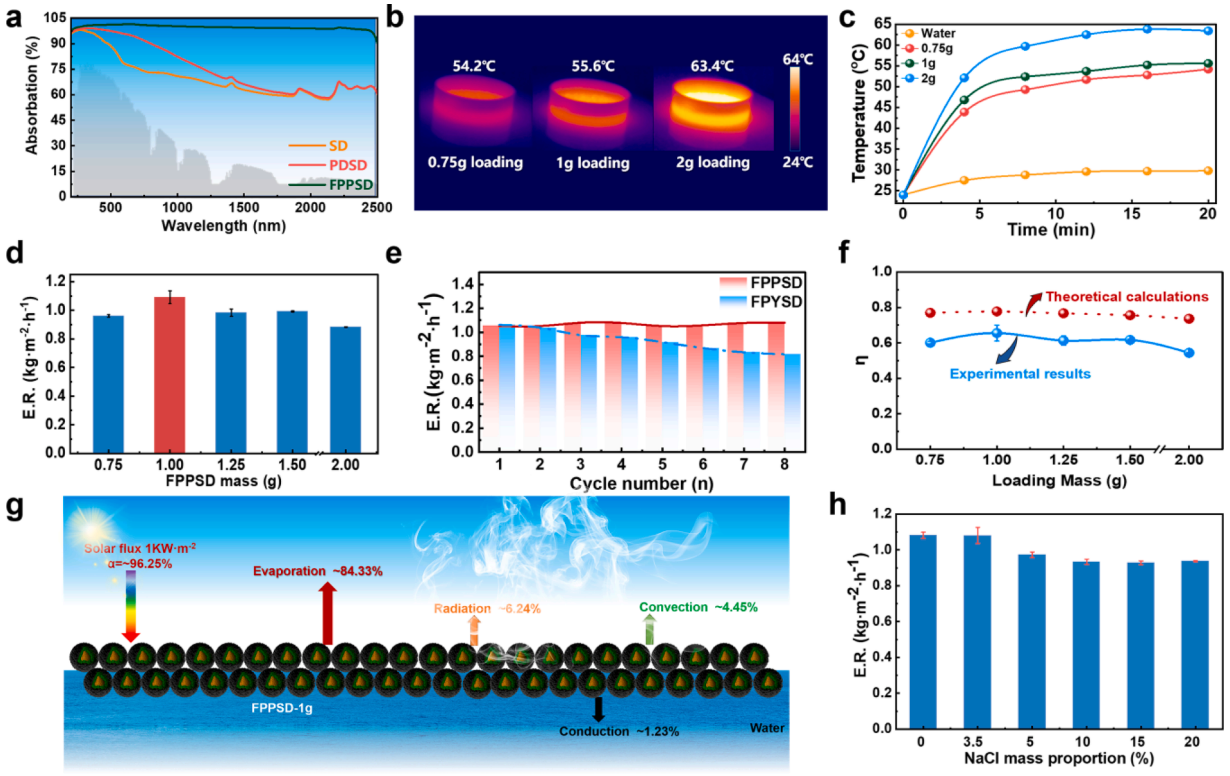

Fig. 3. (a) UV–Vis-IR absorption spectra of SD, PDSD, and FPPSD (wavelength of 400~2500 nm) compared with the standard AM 1.5 G spectral filter (gray). (b) IR thermal images of FPPSD with different masses under the irradiation of one sun. (c) The temperature curves of the water and FPPSD with different masses under one sun. (d) The evaporation rates of the FPPSD with different masses for pure water under one sun. (e) Cyclic photothermal mass change of the FPYSD-1 g and FPPSD-1 g under 1-sun irradiation for 3.5 wt% s salty water. (f) The calculation result of photothermal conversion and evaporation efficiency of the FPPSD for 3.5 wt% s salty water under the irradiation of one sun. (g) Schematic diagram of the heat loss mechanism of the FPPSD-1 g under 1-sun irradiation. (h) The evaporation rates of the FPPSD-1 g for saline water with varying concentrations under the irradiation of one sun.

FPPSD-1 g~1.08 mm, FPPSD-2 g~2.08 mm). Meanwhile, the photothermal conversion ability was gradually enhanced. In addition, the ΔT between the initial and equilibrated temperature was adapted to study the photothermal conversion capacity of the SVGs (Jiang et al., 2016). The ΔT was closely related to the load mass of the FPPSD. With the increase of the FPPSD mass, the surface temperature gradually increased whether it is dry or wet. Moreover, the temperature of the dry state was much higher than that of the wet state due to the heat loss from the water surface (Figs. 3**b, S8**). Furthermore, the ΔT of the FPPSD-1 g was five times more than water, reaching ~55.6 ℃ under 1-sun irradiation (Fig. 3**c**). It should be noted that the load mass of the FPPSD and the low sunlight intensity are two significant factors determining the water evaporation capacity. Too much litter of the FPPSD-0.75 g (0.80 mm) can lead to holes in the FPPSD layer, reducing the overall solar evaporation efficiency. On the contrary, FPPSD-2 g (2.08 mm) can give rise to lower photothermal conversion capacity and unnecessary heat conduction inside the FPPSD layer (Chen et al., 2020b; Zhang et al., 2020). Consequently, the FPPSD-1 g (1.08 mm) exhibited the maximum evaporation rate (1.09 ± 0.04 kg m^{-2} h^{-1}), 3.5 times larger than that of the pure water (~0.31 kg m^{-2} h^{-1}) (**Fig. S9a**). Moreover, the photothermal capacity of the FPPSD evaporator gradually increased with the increase of the light intensity. The evaporation rate of the FPPSD-1 g reached 1.09 ± 0.04 kg m^{-2} h^{-1} under 1-sun irradiation (Figs. 3**d, S9b**). The contribution of the evaporation enthalpy to solar evaporation was also important (Wei et al., 2023). The surface temperature of FPPSD-1 g was ~55.6 ℃ during the evaporation process. Therefore, its evaporation enthalpy was calculated as ~2362.786 kJ·kg^{-1}.

The stability of the photothermal evaporation performance of the FPPSD-1 g was further surveyed. Fig. 3**e** demonstrated that the evaporation rate of the FPPSD-1 g was almost identical to the previous result under 1-sun irradiation after eight cyclic photothermal processes. It should be pointed out that both the evaporation rate and evaporation durability of the FPYSD-1 g were lower than that of FPPSD-1 g under the same condition, indicating the stable photothermal structure of the FPYSD. Moreover, the solar-to-thermal capacity of the FPPSD was calculated according to the energy conversion principle (η) that the absorbed heat could be transformed into many forms, such as heat loss to the ambient environment, radiative, evaporation, convective, and conductive heat loss to the water phase (Zhang et al., 2022b). As shown in Fig. 3**f and g,** the experimental results of the FPPSD have the same trend as the theoretical results calculated from the heat loss model (**Section S2**). Moreover, Fig. 3**f** indicated that the η of the FPPSD increased firstly and then descended with the increasing mass of FPPSD. Thus, the FPPSD-1 g was endowed with the highest conversion efficiency with η of ~67.57 %, which was slightly lower than that of the theoretical calculation.

3.3. *Salt-resistance stability*

The FPPSD evaporator was explored for evaporation because of its unique light absorption capacity. Fig. 3**h** demonstrated that the evaporation rates of the FPPSD-1 g were 1.09 ± 0.01 kg/m^2/h, 0.98 ± 0.01 kg/m^2/h, 0.97 ± 0.01 kg/m^2/h, 0.93 ± 0.02 kg/m^2/h, 0.93 ± 0.01 kg/m^2/h under the condition the concentration of NaCl solution was 3.5 %, 5 %, 10 %, 15 %, and 20 %, respectively. Moreover, after the cyclic evaporation, the FPPSD-1 g evaporator almost maintained its performance for 3.5 wt% saline water under 1-sun illumination (Fig. 4**a**). Meanwhile, the concentrations of the Na^+, K^+, Ca^{2+}, and Mg^{2+} ions were significantly reduced by > 99.2 %, which was substantially less than those of the standards of the World Health Organization (Fig. 4**b**)

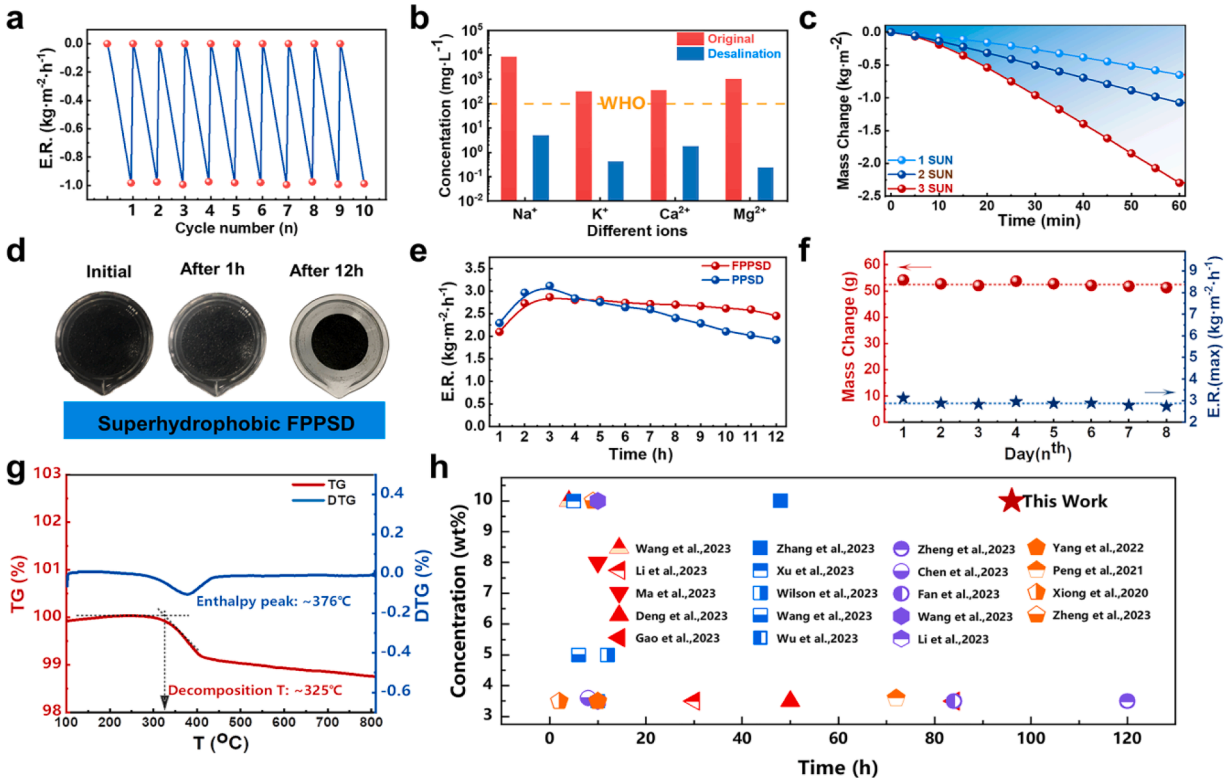

Fig. 4. (a) Cyclical evaporation of the FPPSD-1 g for 3.5 wt% saline water under one sun. (b) Ion contents in the simulated seawater before and after the evaporation of the FPPSD-1 g for 3.5 wt% saline water under one sun. (c) The evaporation rates of the FPPSD-1 g for 10 wt% saline water under different sun illuminations. (d) The photographs of the FPPSD-1 g for 10 wt% saline water and the salt absorption process under 3-sun illumination. (e) The continuous evaporation rates of the FPPSD-1 g and PPSD-1 g for 10 wt% saline water under 3-sun illumination. (f) The continuous evaporation performance of the FPPSD-1 g for 10 wt% saline water under 3-sun illumination. (g) TG and DTG curves of the FPPSD-1 g. (h) The comparison of different previous evaporations reported and this work for their salt-resistant performance.

(Ping et al., 2022). The distinguished salt-rejecting ability benefited from the superhydrophobic property of the FPPSD evaporator.

Besides, the FPPSD evaporator presented excellent solar-to-thermal capacity under different illuminations. The maximum surface temperature of the FPPSD evaporator can reach up to ~56.8 ℃, ~67.6 ℃ and ~85.3 ℃ under the illumination of 1~3 suns, respectively (**Fig. S10**). Correspondingly, the evaporation rates of the FPPSD evaporator achieved 0.65 kg/m^2/h, 1.07 kg/m^2/h, and 2.29 kg/m^2/h for 10 wt% saline water, respectively (Fig. 4**c**). Moreover, after a 12-hour photothermal evaporation process for 10 wt% salty water under 3-sun illumination, salt aggregation occurred on the surface of the hydrophobic PPSD evaporator but not on the superhydrophobic FPPSD evaporator (Figs. 4**d and S11**). The superhydrophobic FPPSD evaporator almost kept its initial photothermal evaporation performance for 10 wt% saline water under 3-sun illumination (Fig. 4**e**). Furthermore, the FPPSD evaporator can achieve excellent continuous evaporation performance with an average photothermal evaporation rate and daily water volume of 2.88 kg/m^2/h and 56.8 g for 10 wt% saline water under 3-sun illumination (Fig. 4**f**). The excellent photothermal performance was under the joint of superhydrophobic intrinsic property and thermal stability of the FPPSD. The former gave this evaporator excellent salt-resistance capacity, and the latter provided a stable structure for the FPPSD evaporator to carry out photothermal water extraction under higher temperatures, as displayed in Fig. 4**g,** with the maximum decomposition temperature up to ~325 ℃. Consequently, the salt-resistance ability of the FPPSD evaporator was far beyond most of the state-of-the-art reported evaporators (Fig. 4**h, Table S2**) (Chen et al., 2023b; Deng et al., 2023; Fan et al., 2023; Gao et al., 2023; Li et al., 2023c, 2023a; Ma et al., 2023; Peng et al., 2021; Wang et al., 2023e; Wilson et al., 2023; Wang et al., 2023a; Wu et al., 2023; Wang et al., 2023c; Xiong et al., 2020; Xu et al., 2023b; Yang et al., 2022; Zhang et al., 2023a; Zheng et al., 2023).

3.4. Environmental stability

The environmental stability of the FPPSD evaporator under different harsh environments is essential for further application. Hence, the durability of the FPPSD evaporator was further estimated by studying the micromorphology structure and wettability. As shown in **Fig. S12,** the PPSD evaporator cannot kept its initial micromorphology and chemical element. Surprisingly, the FPPSD evaporator kept its initial micro/nanostructure even after being treated with NaOH (pH=14), H_2SO_4 (pH=0), BSA (1 wt%), glucose (5 wt%) and HA (1 wt%) for 30 days (Fig. 5**a**).

Furthermore, the FPPSD evaporator maintained the superhydrophobic property under these harsh conditions, demonstrating its stable core-shell structure (Fig. 5**b**). The FPPSD evaporator presented stable solar desalination capability for 3.5 wt% saline water under one sun (Fig. 5**c** and **d**). In addition, it showed excellent environmental stability compared with the evaporations reported previously, implying its possibility of practical application (**Table S3**). The photothermal evaporation performance of the confined FPPSD evaporator in the actual environment was investigated. As displayed in Fig. 5**e**, the outdoor temperature and light intensity changed frequently. The maximum temperature and light intensity reached ~30.7 ℃ and ~1.05-sun. Under this environment, steam was continuously generated from the FPPSD evaporator surface, and a sealed chamber was designed to collect distilled water (Fig. 5**f** and **g**). Furthermore, there was no salt crystallization on the surface of the FPPSD evaporator, demonstrating it can effectively manage pure water during the practical application of photothermal evaporation (Fig. 5 **and h**).

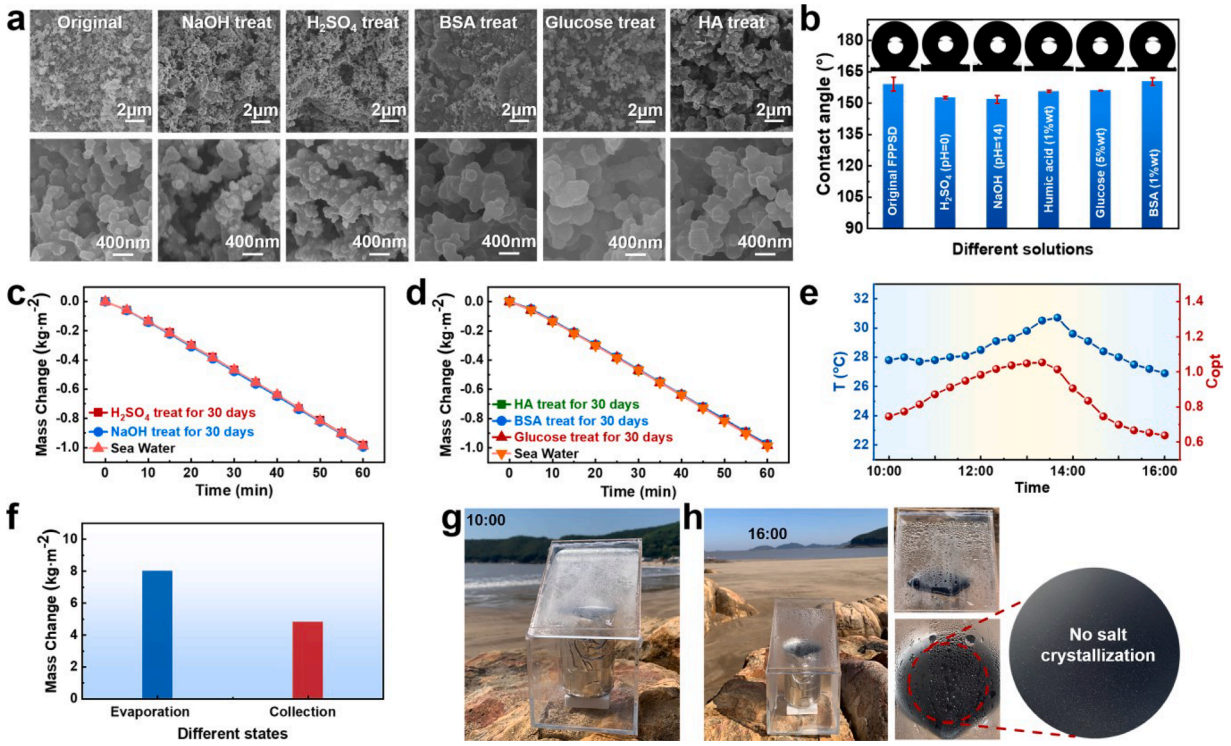

Fig. 5. (a) SEM images and the corresponding enlarged images of the original FPPSD and the treated FPPSD under different conditions, including NaOH (pH=14), H_2SO_4 (pH=0), BSA (1 wt%), glucose (5 wt%) and HA (1 wt%). (b) WCA of the original FPPSD and the treated FPPSD under different conditions. (c) Photothermal evaporation performance of the FPPSD evaporator after the treatment of NaOH (pH=14) and H_2SO_4 (pH=0) for 30 days. (d) Photothermal evaporation performance of the FPPSD evaporator after the treatment of BSA (1 wt%), glucose (5 wt%), and HA (1 wt%) for 30 days. (e) Outdoor temperature and light intensity (Ningbo Xiangshan Dong Dan Beach, China, May 8, 2023). (f) The amount of water evaporated and collected outdoors. (g and h) Outdoor photothermal evaporation experiment.

4. Conclusions

The emerging solar-driven interfacial desalination provides an opportunity for settling the global freshwater crisis. Nonetheless, the salt accumulation inevitably blocks the channel of steam evaporation. It reduces the service period of the solar absorber, leading to a deterioration of the evaporation performance and long-term stability. Here, a novel FPPSD evaporator was constructed by functionalizing PDA, PPy, and PFDTS on the sand surface through π-π conjugation and multiple hydrogen bonding effects. For one thing, the specific collective behaviors of the sands can generate desirable capillary force to supply effective water-pumping channels. Introducing the PFDTS with low surface free energy also gave the FPPSD excellent salt-resistance performance. Meanwhile, the core-shell structure of the FPPSD was designed ingeniously to manage micro-grade water transport and improve environmental stability. Under the function of water steam management and core-shell system, the FPPSD evaporator exhibited a transcendental salt-resistant property with no salt accumulation on its surface even in 10 wt% brine for continuous 96 h illuminations under 3-sun illumination, better than the results of the reported works. Furthermore, this FPPSD evaporator demonstrated outstanding environmental stability that kept its initial core-shell structure, wettability, and water transport capacity even after being treated with harsh operating conditions for 30 days. In addition, outdoor experiments demonstrated clean water collecting ability and excellent salt-resistance ability. With excellent salt resistance and stable environmental stability of the FPPSD evaporator, this design will hold an attractive platform for sustainable solar-driven desalination.

CRediT authorship contribution statement

Qingyang Xue: Methodology, Data curation, Investigation. **Peng Xiao:** Investigation, Data curation. **Jincui Gu:** Writing – original draft, Supervision. **Wenqin Wang:** Writing – original draft. **Luke Yan:** Supervision. **Tao Chen:** Writing – review & editing, Supervision, Conceptualization.

Declaration of competing interest

The authors declare that they have no known competing financial interests or personal relationships that could have appeared to influence the work reported in this paper.

Data availability

Data will be made available on request.

Acknowledgments

This work was supported by National Key Research and Development Program (2022YFC2805202), Ningbo Science and Technology Bureau (2021Z127), Natural Science Foundation of China (52373094), Ningbo Natural Science Foundation (2022J286).

Supplementary materials

Supplementary material associated with this article can be found, in the online version, at doi:10.1016/j.watres.2024.121290.

References

Cao, S., Thomas, A., Li, C., 2023. Emerging materials for interfacial solar-driven water purification. Angew. Chem. Int. Ed. 62 (8), e202214391.

Chen, B., Liu, L., Song, Y., Liu, H., Gong, Z., She, Y., Liu, J., Niu, R., Gong, J., 2023a. Functional upcycling of waste polyester into Cr-MOF towards synergistic interfacial solar evaporation and organic pollutant degradation. Mater. Today Sustain. 24, 100561.
Chen, J., Yin, J.L., Li, B., Ye, Z., Liu, D., Ding, D., Qian, F., Myung, N.V., Zhang, Q., Yin, Y., 2020a. Janus evaporators with self-recovering hydrophobicity for salt-rejecting interfacial solar desalination. ACS Nano 14 (12), 17419–17427.
Chen, G., Sun, J., Peng, Q., Sun, Q., Wang, G., Cai, Y., Gu, X., Shuai, Z., Tang, B.Z., 2020b. Biradical-featured stable organic-small-molecule photothermal materials for highly efficient solar-driven water evaporation. Adv. Mater. 32 (29), 1908537.
Chen, H., Pan, G., Yan, M., Wang, F., Wu, Y., Guo, C., 2023b. Janus membrane with enhanced interfacial activation for solar evaporation. J. Energy Chem. 87, 1–11.
Cheng, P., Wang, D., Schaaf, P., 2022. A review on photothermal conversion of solar energy with nanomaterials and nanostructures: from fundamentals to applications. Adv. Sustain. Syst. 6 (10), 2200115.
Deng, D., Liang, Q., Xiao, Z., Liu, C., 2023. Novel solar evaporator with closely-stacked reverse U-shaped hydrogel tubes for long-term stable evaporation with excellent salt resistance. Chem. Eng. J. 474, 145422.
Ding, T., Zhou, Y., Ong, W.L., Ho, G.W., 2021. Hybrid solar-driven interfacial evaporation systems: beyond water production towards high solar energy utilization. Mater. Today 42, 178–191.
Dong, Y.M., Tan, Y., Wang, K.L., Cai, Y.H., Li, J.Z., Sonne, C., Li, C., 2022. Reviewing wood-based solar-driven interfacial evaporators for desalination. Water Res. 223, 119011.
Fan, X., Peng, Y., Lv, B., Yang, Y., You, Z., Song, C., Xu, Y., 2023. A siphon-based spatial evaporation device for efficient salt-free interfacial steam generation. Desalination 552, 116442.
Fan, Y.K., Bai, W., Mu, P., Su, Y.N., Zhu, Z.Q., Sun, H.X., Liang, W.D., Li, A., 2020. Conductively monolithic polypyrrole 3-D porous architecture with micron-sized channels as superior salt-resistant solar steam generators. Sol. Energy Mat. Sol. C 206, 110347.
Gao, Y., Sun, Q., Chen, Y., Zhou, X., Wei, C., Lyu, L., 2023. A highly efficient bio-inspired 3D solar-driven evaporator with advanced heat management and salt fouling resistance design. Chem. Eng. J. 455, 140500.
Greczynski, G., Hultman, L., 2020. X-ray photoelectron spectroscopy: towards reliable binding energy referencing. Prog. Mater Sci. 107, 100591.
Hu, T., Li, L., Yang, Y., Zhang, J., 2020. A yolk@shell superhydrophobic/superhydrophilic solar evaporator for efficient and stable desalination. J. Mater. Chem. A 8, 14736–14745.
Huang, Z., Liu, Y., Li, S., Lee, C.S., Zhang, X.H., 2022. From materials to devices: rationally designing solar steam system for advanced applications. Small Methods 6 (10), 2200835.
Jia, J., Liang, W.D., Sun, H.X., Zhu, Z.Q., Wang, C.J., Li, A., 2019. Fabrication of bilayered attapulgite for solar steam generation with high conversion efficiency. Chem. Eng. J. 361, 999–1006.
Jiang, Q., Tian, L., Liu, K.K., Tadepalli, S., Raliya, R., Biswas, P., Naik, R.R., Singamaneni, S., 2016. Bilayered biofoam for highly efficient solar steam generation. Adv. Mater. 28 (42), 9400–9407.
Lai, X., Hu, J., Qu, J., 2023. Achieving lasting corrosion protection for superhydrophobic epoxy coatings with photothermal conversion property via constructing functionalized graphene nanoplatelet. Carbon N. Y. 212, 118155. Carbon. N. Y.
Lazar, P., Mach, R., Otyepka, M., 2019. Spectroscopic fingerprints of graphitic, pyrrolic, pyridinic, and chemisorbed nitrogen in N-doped graphene. J. Phys. Chem. C 123 (16), 10695–10702.
Li, Z., Xu, X., Sheng, X., Lin, P., Tang, J., Pan, L., Kaneti, Y.V., Yang, T., Yamauchi, Y., 2021a. Solar-powered sustainable water production: state-of-the-art technologies for sunlight-energy-water nexus. ACS Nano 15 (8), 12535–12566.
Li, D., Liang, Z., Yang, H., Zhang, M., Cao, K., Zhao, B., Wang, Y., Peng, M., Sun, Y., Jiang, L., 2023a. Mutual reinforcement of evaporation and catalysis for efficient freshwater-salt-chemical production. Adv. Funct. Mater., 2300353
Li, L., He, N., Jiang, B., Yu, K., Zhang, Q., Zhang, H., Tang, D., Song, Y., 2021b. Highly salt-resistant 3D hydrogel evaporator for continuous solar desalination via localized crystallization. Adv. Funct. Mater. 31 (43), 2104380.
Li, H.N., Yang, H.C., Zhu, C.Y., Wu, J., Greiner, A., Xu, Z.K., 2022. A self-descaling Janus nanofibrous evaporator enabled by a “moving interface” for durable solar-driven desalination of hypersaline water. J. Mater. Chem. A 10 (39), 20856–20865.
Li, X.R., Wang, P.X., Lu, Q.Y., Yao, H.Z., Yang, C., Zhao, Y.M., Hu, J.Y., Zhou, H.F., Song, M.Y., Cheng, H.H., Dai, H.L., Wang, X.G., Geng, H.Y., 2023b. A hierarchical porous aerohydrogel for enhanced water evaporation. Water Res. 244, 120447.
Li, Y., Chen, N., Li, Z., Shao, H., Sun, X., Liu, F., Liu, X., Guo, Q., Qu, L., 2021c. Reborn three-dimensional graphene with ultrahigh volumetric desalination capacity. Adv. Mater. 33 (48), 2105853.
Li, Y., Cheng, S., Jin, B., Yu, Z., Gu, R., 2023c. Extendable solar interfacial evaporator with high salt resistance achieved by managing the evaporation region. Sol. RRL 7 (13), 2300242.
Lin, Q., Yang, Y., Ma, Y., Zhang, R., Wang, J., Chen, X., Shao, Z., 2018. Bandgap engineered polypyrrole-polydopamine hybrid with intrinsic raman and photoacoustic imaging contrasts. Nano Lett. 18 (12), 7485–7493.
Lu, Q., Shi, W., Yang, H., Wang, X., 2020. Nanoconfined water-molecule channels for high-yield solar vapor generation under weaker sunlight. Adv. Mater. 32 (42), 2001544.
Ma, W., Lu, T., Cao, W., Xiong, R., Huang, C., 2023. Bioinspired nanofibrous aerogel with vertically aligned channels for efficient water purification and salt-rejecting solar desalination. Adv. Funct. Mater. 33 (23), 2214157.
Mo, H.T., Wang, Y., 2022. A bionic solar-driven interfacial evaporation system with a photothermal-photocatalytic hydrogel for VOC removal during solar distillation. Water Res. 226, 119276.
Mu, P., Bai, W., Fan, Y.K., Zhang, Z., Sun, H.X., Zhu, Z.Q., Liang, W.D., Li, A., 2019a. Conductive hollow kapok fiber-PPy monolithic aerogels with excellent mechanical robustness for efficient solar steam generation. J. Mater. Chem. A 7 (16), 9673–9679.
Mu, P., Zhang, Z., Bai, W., He, J.X., Sun, H.X., Zhu, Z.Q., Liang, W.D., Li, A., 2019b. Superwetting monolithic hollow-carbon-nanotubes aerogels with hierarchically nanoporous structure for efficient solar steam generation. Adv. Energy Mater. 9 (1), 1802158.
Ni, F., Xiao, P., Qiu, N., Zhang, C., Liang, Y., Gu, J., Xia, J., Zeng, Z., Wang, L., Xue, Q., Chen, T., 2020. Collective behaviors mediated multifunctional black sand aggregate towards environmentally adaptive solar-to-thermal purified water harvesting. Nano Energy 68, 104311.
Pan, X.F., Bao, Z., Xu, W., Gao, H.L., Wu, B., Zhu, Y., Yu, G.H., Chen, J., Zhang, S.C., Li, L., Wu, H.A., Li, X., Yu, S.H., 2023. Recyclable nacre-like aramid-mica nanopapers with enhanced mechanical and electrical insulating properties. Adv. Funct. Mater. 33 (9), 2210972.
Park, S.J., Seo, M.K., Lee, Y.S., 2003. Surface characteristics of fluorine-modified PAN-based carbon fibers. Carbon N. Y. 41 (4), 723–730. Carbon. N. Y.
Paternò, G.M., Chen, Q., Muñoz-Mármol, R., Guizzardi, M., Bonal, V., Kabe, R., Barker, A.J., Boj, P.G., Chatterjee, S., Ie, Y., Villalvilla, J.M., Quintana, J.A., Scotognella, F., Müllen, K., Díaz-García, M.A., Narita, A., Lanzani, G., 2022. Excited states engineering enables efficient near-infrared lasing in nanographenes. Mater. Horiz. 9 (1), 393–402.
Peng, F., Xu, J., Bai, X., Feng, G., Zeng, X., Ibn Raihan, M.R., Bao, H., 2021. A Janus solar evaporator with 2D water path for highly efficient salt-resisting solar steam generation. Sol. Energy Mat. Sol. C. 221, 110910.
Ping, Z., Fang, H., Wang, K., Zhang, H., Li, S., Chen, J., Huang, F., 2022. A universal Cl-PEDOT coating strategy based on oxidative chemical vapor deposition toward solar-driven multifunctional energy management. Adv. Funct. Mater. 32 (51), 2208965.
Razaqpur, A.G., Wang, Y.Q., Liao, X.J., Liao, Y., Wang, R., 2021. Progress of photothermal membrane distillation for decentralized desalination: a review. Water Res. 201, 117299.
Shen, C., Zhu, Y., Xiao, X., Xu, X., Chen, X., Xu, G., 2020. Economical salt-resistant superhydrophobic photothermal membrane for highly efficient and stable solar desalination. ACS Appl. Mater. Interfaces 12 (31), 35142–35151.
Shi, Y., Ilic, O., Atwater, H.A., Greer, J.R., 2021. All-day fresh water harvesting by microstructured hydrogel membranes. Nat. Commun. 12 (1), 2797.
Tao, P., Ni, G., Song, C., Shang, W., Wu, J., Zhu, J., Chen, G., Deng, T., 2018. Solar-driven interfacial evaporation. Nat. Energy 3 (12), 1031–1041.
Thakur, V.K., Vennerberg, D., Kessler, M.R., 2014. Green aqueous surface modification of polypropylene for novel polymer nanocomposites. ACS Appl. Mater. Interfaces 6 (12), 9349–9356.
Wang, S., Xiao, C., Lu, S., Lu, H., Hasi, Q.M., Zhang, Y., Luo, X., Chen, L., 2023a. Integrated solar evaporator with salt resistance and lipophobicity derived from waste newspapers for efficient desalination. ACS Sustain. Chem. Eng. 11 (6), 2586–2598.
Wang, Y., Sun, X., Tao, S., 2020. Rational 3D coiled morphology for efficient solar-driven desalination. Environ. Sci. Technol. 54 (24), 16240–16248.
Wang, Y., Li, S., Wu, X., Zhang, J., Feng, J., Li, M., Zong, S., Yan, W., 2023b. Nitrogen-based conjugated microporous polymers for efficient Hg(II) removal from water: performance and mechanism. Chem. Eng. J. 471, 144659.
Wang, Y., Gu, F.Q., Ni, L.J., Liang, K., Marcus, K., Liu, S.L., Yang, F., Chen, J.J., Feng, Z. S., 2017. Easily fabricated and lightweight PPy/PDA/AgNW composites for excellent electromagnetic interference shielding. Nanoscale 9 (46), 18318–18325. Nanoscale.
Wang, Z., Wu, X., He, F., Peng, S., Li, Y., 2021a. Confinement capillarity of thin coating for boosting solar-driven water evaporation. Adv. Funct. Mater. 31 (22), 2011114.
Wang, L., Liu, Z., Xu, J., Wang, K., Wang, Q., Liu, G., 2023c. Conical solar-thermo-radiative evaporator for sustainable desalination and salt recovery. Desalination 567, 116993.
Wang, X., Sun, Y., Zhao, G.Y., Wang, X.Z., Qiu, J.S., 2023d. Preparation of carbon nanotube/cellulose hydrogel composites and their uses in interfacial solar-powered water evaporation. New Carbon Mater. 38 (1), 162–172.
Wang, C., Xu, K., Shi, G., Wei, D., 2023e. Water skin effect and arched double-sided evaporation for boosting all-weather high salinity desalination. Adv. Energy Mater. 13 (21), 2300134.
Wang, S., Fan, Y.K., Wang, F., Su, Y.N., Zhou, X., Zhu, Z.Q., Sun, H.X., Liang, W.D., Li, A., 2021b. Potentially scalable fabrication of salt-rejection evaporator based on electrogenerated polypyrrole-coated nickel foam for efficient solar steam generation. Desalination 505, 114982.
Wei, D., Wang, C., Zhang, J., Zhao, H., Asakura, Y., Eguchi, M., Xu, X., Yamauchi, Y., 2023. Water activation in solar-powered vapor generation. Adv. Mater. 35 (47), 2212100.
Wilson, H.M., Suh, Y., Lim, H.W., Raheman, A.R., S, Lee, S.J., 2023. A low-cost plant transpiration inspired 3D popsicle design for highly efficient solar desalination. Desalination 563, 116731.
Wu, L., Dong, Z., Cai, Z., Ganapathy, T., Fang, N.X., Li, C., Yu, C., Zhang, Y., Song, Y., 2020. Highly efficient three-dimensional solar evaporator for high salinity desalination by localized crystallization. Nat. Commun. 11 (1), 521.
Wu, J., Zhang, T., Qu, J., Jiao, F.Z., Hu, C., Zhao, H.Y., Li, X., Yu, Z.Z., 2023. Hydrothermally modified 3D porous loofah sponges with MoS_2 sheets and carbon particles for efficient solar steam generation and seawater desalination. ACS Appl. Mater. Interfaces 15 (24), 29457–29467.

Xie, H., Du, Y., Zhou, W., Xu, W., Zhang, C., Niu, R., Wu, T., Qu, J., 2023. Efficient fabrication of micro/nanostructured polyethylene/carbon nanotubes foam with robust superhydrophobicity, excellent photothermality, and sufficient adaptability for all-weather freshwater harvesting. Small 19 (28), 2300915.
Xie, H., Xu, W.H., Du, Y., Gong, J., Niu, R., Wu, T., Qu, J.P., 2022. Cost-effective fabrication of micro-nanostructured superhydrophobic polyethylene/graphene foam with self-floating, optical trapping, acid-/alkali resistance for efficient photothermal deicing and interfacial evaporation. Small 18 (17), 2200175.
Xing, H., Song, Y., Xu, H., Chen, S., Li, K., Dong, L., Wang, B., Xue, J., Lu, Y., 2023. A magneto-heated silk fibroin scaffold for anti-biofouling solar steam generation. Small 19 (18), 2206189.
Xiong, Z.C., Zhu, Y.J., Qin, D.D., Yang, R.L., 2020. Flexible salt-rejecting photothermal paper based on reduced graphene oxide and hydroxyapatite nanowires for high-efficiency solar energy-driven vapor generation and stable desalination. ACS Appl. Mater. Interfaces 12 (29), 32556–32565.
Yu, H., Wang, D., Jin, H., Wu, P., Wu, X., Chu, D., Lu, Y., Yang, X., Xu, H., 2023. 2D $MoN_{1.2}$-rGO stacked heterostructures enabled water state modification for highly efficient interfacial solar evaporation. Adv. Funct. Mater. 33 (24), 2214828.
Xu, K., Wang, C., Li, Z., Wu, S., Wang, J., 2021. Salt mitigation strategies of solar-driven interfacial desalination. Adv. Funct. Mater. 31 (8), 2007855.
Xu, N., Zhu, P., Sheng, Y., Zhou, L., Li, X., Tan, H., Zhu, S., Zhu, J., 2020. Synergistic tandem solar electricity-water generators. Joule 4 (2), 347–358.
Xu, Z., Ran, X., Zhang, Z., Zhong, M., Wang, D., Li, P., Fan, Z., 2023a. Designing a solar interfacial evaporator based on tree structures for great coordination of water transport and salt rejection. Mater. Horiz. 10 (5), 1737–1744.
Xu, Z., Yang, Y., Ye, C., Lin, X., Shen, J., Ye, M., 2023b. Salt-resistance holocellulose-based solar steam evaporator for desalination brine water. J. Environ. Chem. Eng. 11 (5), 110634.
Yang, H.C., Lu, F., Li, H.N., Zhang, C., Darling, S.B., Xu, Z.K., 2023a. Membranes in solar-driven evaporation: design principles and applications. Adv. Funct. Mater. 33 (43), 2304580.
Yang, H., Sun, Y., Peng, M., Cai, M., Zhao, B., Li, D., Liang, Z., Jiang, L., 2022. Tailoring the salt transport flux of solar evaporators for a highly effective salt-resistant desalination with high productivity. ACS Nano 16 (2), 2511–2520.
Yang, P., Zhu, F., Zhang, Z., Cheng, Y., Wang, Z., Li, Y., 2021. Stimuli-responsive polydopamine-based smart materials. Chem. Soc. Rev. 50 (14), 8319–8343.
Yang, P., Bai, W., Zou, Y., Zhang, X., Yang, Y., Duan, G., Wu, J., Xu, Y., Li, Y., 2023b. A melanin-inspired robust aerogel for multifunctional water remediation. Mater. Horiz. 10 (3), 1020–1029.
Zhang, C., Xiao, P., Ni, F., Gu, J., Chen, J., Nie, Y., Kuo, S.W., Chen, T., 2022a. Breathable and superhydrophobic photothermic fabric enables efficient interface energy management via confined heating strategy for sustainable seawater evaporation. Chem. Eng. J. 428, 131142.
Zhang, C., Shi, Y., Shi, L., Li, H., Li, R., Hong, S., Zhuo, S., Zhang, T., Wang, P., 2021a. Designing a next generation solar crystallizer for real seawater brine treatment with zero liquid discharge. Nat. Commun. 12 (1), 998.
Zhang, Z., Mu, P., He, J.X., Zhu, Z.Q., Sun, H.X., Wei, H.J., Liang, W.D., Li, A., 2019. Facile and scalable fabrication of surface-modified sponge for efficient solar steam generation. ChemSusChem 12 (2), 426–433. ChemSusChem.
Zhao, F., Guo, Y., Zhou, X., Shi, W., Yu, G., 2020. Materials for solar-powered water evaporation. Nat. Rev. Mater. 5 (5), 388–401.
Zou, H., Meng, X., Zhao, X., Qiu, J., 2023. Hofmeister effect-enhanced hydration chemistry of hydrogel for high-efficiency solar-driven interfacial desalination. Adv. Mater. 35 (5), 2207262.
Zhao, H.Y., Huang, J., Zhou, J., Chen, L.F., Wang, C., Bai, Y., Zhou, J., Deng, Y., Dong, W. X., Li, Y.S., Yu, S.H., 2022. Biomimetic design of macroporous 3D truss materials for efficient interfacial solar steam generation. ACS Nano 16 (3), 3554–3562.
Zhang, H., Du, Y., Jing, D., Yang, L., Ji, J., Li, X., 2023a. Integrated Janus evaporator with an enhanced donnan effect and thermal localization for salt-tolerant solar desalination and thermal-to-electricity generation. ACS Appl. Mater. Interfaces. 15 (42), 49892–49901.
Zang, L.L., Finnerty, C., Zheng, S.X., Conway, K., Sun, L.G., Ma, J., Mi, B.X., 2021. Interfacial solar vapor generation for desalination and brine treatment: evaluating current strategies of solving scaling. Water Res. 198, 117135.
Zhang, L., Zhang, Y., Zou, M., Yu, C., Li, C., Gao, C., Dong, Z., Wu, L., Song, Y., 2023b. A bionic-gill 3D hydrogel evaporator with multidirectional crossflow salt mitigation and aquaculture applications. Adv. Funct. Mater. 33 (24), 2300318.
Zhang, L., Mu, L., Zhou, Q., Hu, X., G, X., 2020. Solar-assisted fabrication of dimpled 2H-MoS_2 membrane for highly efficient water desalination. Water Res. 170, 115367.
Zhang, R., Xiang, B., Wang, Y., Tang, S., Meng, X., 2022b. A lotus-inspired 3D biomimetic design toward an advanced solar steam evaporator with ultrahigh efficiency and remarkable stability. Mater. Horiz. 9 (4), 1232–1242.
Zheng, S.Y., Zhou, J., Si, M., Wang, S., Zhu, F., Lin, J., Fu, J., Zhang, D., Yang, J., 2023. A molecularly engineered zwitterionic hydrogel with strengthened anti-polyelectrolyte effect: from high-rate solar desalination to efficient electricity generation. Adv. Funct. Mater. 33 (43), 2303272.
Zhang, W., Wang, D., Sun, Z., Song, J., Deng, X., 2021b. Robust superhydrophobicity: mechanisms and strategies. Chem. Soc. Rev. 50 (6), 4031–4061.
Zou, M., Zhang, Y., Cai, Z., Li, C., Sun, Z., Yu, C., Dong, Z., Wu, L., Song, Y., 2021. 3D printing a biomimetic bridge-arch solar evaporator for eliminating salt accumulation with desalination and agricultural applications. Adv. Mater. 33 (34), 2102443.